J̸M PAPERS

Dynamics of an inertially collapsing gas bubble between two parallel, rigid walls

Mauro Rodriguez Jr[1],†, **Shahaboddin A. Beig**[2], **Charlotte N. Barbier**[3] **and Eric Johnsen**[2]

[1]School of Engineering, Brown University, Providence, RI 02912, USA

[2]Department of Mechanical Engineering, University of Michigan, Ann Arbor, MI 48109, USA

[3]Oak Ridge National Laboratory, Oak Ridge, TN 37830, USA

The collapse of cavitation bubbles in channel flows can give rise to structural damage along neighbouring walls. Although the collapse of a bubble near a single wall has been studied extensively, less is known about bubble collapse between two walls, e.g. as in a channel. We conduct highly resolved, direct simulations of the Navier–Stokes equations to investigate the bubble dynamics and pressures produced by the collapse of a bubble between two parallel rigid walls. We examine the dependence of the dynamics and pressures on the initial bubble location, confinement and driving pressure. For a fixed initial stand-off distance, as the channel width increases the bubble volume, migration distance and re-entrant jet speed approach their single-wall counterparts. We obtain an expression for the minimum channel width at which the confinement does not affect the bubble dynamics depending on the driving pressure difference and initial stand-off distance. For a fixed channel width, varying stand-off distance reduced the maximum wall pressures in the channel relative to the single wall; the trend was consistent for three different driving pressures. Two different jetting behaviours are seen when the bubble is centred in the channel, depending on the channel width. Under significant confinement, wall-parallel re-entrant jets impinge upon each other and further intensify the collapse of the vortex ring.

Key words: bubble dynamics, cavitation, computational methods

1. Introduction

Cavitation-bubble collapse and subsequent damage occur in confined geometries (e.g. in channels, pipes and other enclosed systems) in various hydraulic and engineering applications, including in therapeutic ultrasound procedures such as shock-wave

† Email address for correspondence: mauro_rodriguez@brown.edu

lithotripsy, fuel injectors, thermal-hydraulic systems and the spallation neutron source (SNS). With regard to the latter, cavitation erosion is the lifetime-limiting factor for the target used in the SNS at the Oak Ridge National Laboratory (Haines *et al.* 2014; Riemer *et al.* 2014) and in similar proton beam facilities (Futakawa *et al.* 2014; Naoe *et al.* 2016, 2018). Moreover, the channel geometry mitigates cavitation in a mercury target for neutron production (McClintock *et al.* 2012). Negative transient pressures vaporise the working liquid and small vapour bubbles grow rapidly and collapse near solid surfaces. During collapse, a cavitation bubble concentrates energy into the release of an outward-propagating shock wave capable of damaging surrounding solids (Rayleigh 1917; Hickling & Plesset 1964; Benjamin & Ellis 1966). The collapse dynamics, pressures and temperatures experienced by neighbouring surfaces are of key interest to characterise the damage mechanisms and predict mass loss (Franc *et al.* 2012; Kim *et al.* 2014).

Nearby surfaces break the spherical symmetry of a collapsing bubble. The non-spherical dynamics have been extensively examined (Kornfeld & Suvorov 1944; Lauterborn & Bolle 1975; Blake & Gibson 1987; Vogel, Lauterborn & Timm 1989). Compared with a spherical collapse, pressures produced on the nearby surface are attributed to the water-hammer shock wave emitted from the jet impinging upon the opposite side of the bubble, sometimes directly onto the solid surface (Naudé & Ellis 1961; Plesset & Chapman 1971; Tomita & Shima 1986). Scaling relationships for the re-entrant jet speeds and water-hammer shock pressures have been developed as functions of driving pressure and initial bubble stand-off distance from the neighbouring wall (Supponen *et al.* 2016, 2017).

Numerical simulation approaches, including the boundary element and boundary integral methods (Blake, Taib & Doherty 1986; Zhang, Duncan & Chahine 1993; Wang 2014; Aganin *et al.* 2016; Brujan, Takahira & Ogasawara 2019), finite-volume approaches (Sagar & el Moctar 2020) and potential flow calculations (Plesset & Chapman 1971; Molefe & Peters 2019), predict the behaviour of a single bubble collapsing near a wall, re-entrant jet speeds, as well as material pitting (Hsiao *et al.* 2014). However, these approaches assume an incompressible or weakly compressible liquid, such that they cannot capture shock–wall interactions pertinent to cavitation damage. Johnsen & Colonius (2006), Beig & Johnsen (2015), Coralic & Colonius (2013), Schmidmayer, Bryngelson & Colonius (2020), Trummler *et al.* (2020) and Trummler, Schmidt & Adams (2021) conducted simulations of this problem with high-order accurate, shock- and interface-capturing approaches. The numerical simulations of Beig (2018) showed the differences between spherical bubble collapse and collapse near a wall. In the spherical case, the collapse concentrates the available potential energy into the bubble internal energy at minimum volume. The energy is released as a shock whose pressure amplitude decays as $1/r^{1.13}$ (Cole 1948), where r is a given radial distance from the collapse origin. In the case of collapse near a single wall, the pressure produced a given distance away is different from the spherical case, due to (i) a collapse at a different location from the bubble original location (attracted to wall by image bubble), (ii) energy release due to the water-hammer process, (iii) a resulting shock whose strength is greater in the direction of the shock (and weak in other directions along the front). Moreover, results from Beig (2018) showed agreement with experimental re-entrant jet speeds (Brujan *et al.* 2002; Supponen *et al.* 2016), collapse morphology (Philipp & Lauterborn 1998) and the maximum wall pressure scaling.

Bubble dynamics in a confined environment have been investigated in a variety of settings. Past studies examined nonlinear oscillations in spherically confining compliant materials (Vincent *et al.* 2014; Vincent & Marmottant 2017) or in a tube (Oğuz &

Prosperetti 1998; Farhangmehr *et al.* 2014), which may lead to non-spherical behaviour. Dabir-Moghaddam & Wu (2016), using a finite-volume approach, simulated the inertial collapse of a single bubble in a cylinder and observed increased shock pressures from the bubble collapse on the cylindrical wall relative to a single flat wall configuration. Using laser-induced experiments and the boundary-element method, the single bubble collapse between two parallel plates with a vertical plate at the end (Brujan *et al.* 2019; Li *et al.* 2019) or near corner (Brujan *et al.* 2018), has been studied to determine the re-entrant jet angle dependence on the stand-off distances from the plate.

The problem of interest here involves a gas bubble collapsing between two parallel, rigid plates (walls). Gonzalez-Avila *et al.* (2011) studied the cavitation bubble growth and collapse dynamics of a bubble nucleated at one of the channel walls via experiments and a boundary-element method. In the study, the non-dimensional channel width, $\eta_o = W/R_o$, where R_o is the maximum bubble radius and W the channel height or width, was varied from 0.3 to 7.3. Here, we use the same definition for the non-dimensional channel width. For $\eta_o < 2$, the bubble is attached to at least one of the channel walls. The study showed η_o affecting the dynamics, revealing three different collapse scenarios: collapse at the channel centre (neutral collapse); collapse onto the lower wall; and collapse onto upper wall. For large widths $\eta_o > 7$, the far-plate no longer affects the collapse. Using the same configuration, Gonzalez-Avila *et al.* (2019) studied the shear stress fields at the proximal plate and observed enhanced bubble centre migration. Similarly, Zeng, Gonzalez-Avila & Ohl (2020) observed the same aforementioned three different jetting scenarios that strongly depend on η_o and the stand-off distance from the proximal wall, γ_o. Our interests here are on detached bubble configurations, i.e. $\eta_o > 2$, to determine the effect of the far channel wall by comparing with the single-wall configuration. The first studies of this configuration are those of Chahine (1982) and Kuvshinov *et al.* (1982). In particular, Chahine & Morine (1980) observed re-entrant jets forming in the wall-parallel direction through the channel centre for $\eta_o \approx 20/9$. Ishida *et al.* (2001) and Hsiao *et al.* (2013) qualitatively studied this collapse morphology for $\eta_o > 2$ configurations using a boundary-element method. Similarly, Farhangmehr *et al.* (2014) observed the re-entrant jet direction change for $\eta_o \approx 3$ for a bubble collapsing in a cylinder. Using boundary-element and potential flow methods, Kucera & Blake (1990) also observed the wall-parallel jets in a channel and cylinder; however, they noted that these methods may not yield realistic bubble shapes under high confinement. Thus, to accurately capture both the bubble collapse and shock pressures, high-order accurate numerical approaches representing the full compressible dynamics are required.

The objective of this work is to determine the role of confinement on the dynamics and wall impact loads of a single bubble inertially collapsing in a channel via numerical simulation. In addition to the driving pressure and initial stand-off distance in the case of a bubble collapsing near a single wall, we show that the relative size of the bubble to the channel width affects the bubble dynamics (volume and location at collapse, jet speed), and therefore the wall pressure, in the case of collapse between two parallel walls. Though the wall pressures are lower than in the corresponding collapse near a single wall, significant pressures can be produced along the far wall. The paper outline is as follows. The problem set-up, governing equations for binary water-gas compressible, multiphase flows, and numerical solver of Beig, Aboulhasanzadeh & Johnsen (2018) are presented in § 2. In § 3, the bubble dynamics and maximum wall pressures are compared between the channel and single-wall configurations for baseline parameters. We find the approximate channel width and driving pressure where the dynamics approach single-wall values. We then investigate the bubble dynamics and maximum wall pressures dependence on the
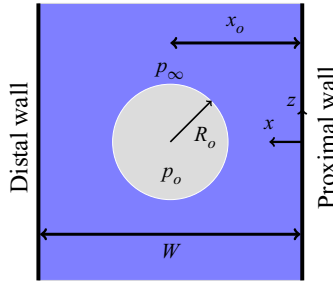
Figure 1. Problem set-up of an inertially collapsing, spherical gas bubble initially at maximum volume between flat, rigid parallel walls (channel). The *y*-axis points into the page.

channel width, initial bubble stand-off distance and driving pressure. Additionally, we discuss the special case of a channel-centred bubble at various confinement and driving pressures. We summarise our findings in § 4.

2. Problem set-up and governing equations

As illustrated in figure 1, our geometry consists of two flat, rigid, infinitely long parallel plates (distal and proximal), a width W from each other. An initially spherical bubble of radius R_o is placed a distance x_o from the proximal plate. As a reference, we take $R_o = 500\,\mu\text{m}$. Liquid water of pressure p_∞ and temperature T_∞ surrounds the bubble. Water vapour in the bubble is modelled as a non-condensable ideal gas with initial pressure $p_o = 3550\,\text{Pa}$ and temperature $T_o = 300\,\text{K}$; the collapse is initiated due to the resulting pressure difference across the bubble interface. Due to the symmetry in the *xz*- and *xy*-plane (i.e. front and bottom planes in figure 1, respectively), a quarter of the domain is simulated with symmetric boundary conditions. The top and back planes have non-reflecting boundary conditions (Thompson 1990). Distal and proximal channel walls are rigid, perfectly reflecting, no-slip boundary conditions; simulations of collapse near a single wall are conducted by prescribing non-reflecting conditions in the place of the distal wall. The computational domain has dimensions $W \times 4R_o \times 4R_o$. A resolution of 192 computational cells per initial bubble radius and grid spacing is fixed for each simulation (i.e. the number of computational points changes with channel width). The dimensions and resolution were determined such that the boundary reflections do not affect the bubble dynamics based on results of Beig *et al.* (2018).

Three non-dimensional parameters are considered in this problem: (i) the channel width η_o; (ii) the initial, bubble centroid stand-off distance with respect to the proximal wall $\gamma_o = x_o/R_o$; and (iii) the driving pressure ratio p_∞/p_{atm} (where p_{atm} is the atmospheric pressure). At collapse (i.e. at minimum volume), the bubble centroid *x*-location, x_c and the non-dimensional bubble collapse location is $\gamma_c = x_c/R_o$. We consider the case $\eta_o = 4$, $\gamma_o = 5/4$ and $p_\infty = 5\,\text{MPa}$, as a baseline case. To understand the role of confinement, we conduct a sequence of simulations varying one of the baseline parameters per sequence. Table 1 tabulates the initial conditions for the simulations. We consider three different driving pressures ($p_\infty = 2$, 5 and 10 MPa), motivated by the cavitation studies of Franc *et al.* (2011) identifying these pressures relevant for cavitation erosion applications. Additionally, we consider seven channel-centred (i.e. $\eta_o = 2\gamma_o$) bubble simulations for each of the driving pressure ratios. For the single-wall simulations, we consider 24 total initial stand-off distances. Time is non-dimensionalised using the Rayleigh collapse time for a bubble in a free field, $t_c = 0.915R_o\sqrt{\rho_\ell/\Delta p}$, where ρ_ℓ is the liquid density

Study	Simulation #	η_o	γ_o	p_∞ (MPa)
Baseline	1	4	5/4	5
η_o	2–8	$3, \frac{7}{2}, \frac{9}{2}, 5, 6, 7, 8$	5/4	5
γ_o	9–17	4	$\frac{17}{16}, \frac{9}{8}, \frac{19}{16}, \frac{11}{8}, \frac{3}{2}, \frac{13}{8}, \frac{7}{4}, \frac{15}{8}, 2$	2
	18–26			5
	27–35			10
$\eta_o = 2\gamma_o$	36–41	$2\gamma_o$	$\frac{17}{16}, \frac{9}{8}, \frac{19}{16}, \frac{5}{4}, \frac{3}{2}, \frac{7}{4}$	2
	42–47			5
	48–53			10
Single wall	54–59	∞	$\frac{17}{16}, \frac{9}{8}, \frac{5}{4}, \frac{3}{2}, 2, 3$	2
	60–70		$\frac{17}{16}, \frac{9}{8}, \frac{19}{16}, \frac{5}{4}, \frac{3}{2}, 2, \frac{5}{2}, 3, \frac{7}{2}, 4, 5$	5
	71–77		$\frac{17}{16}, \frac{9}{8}, \frac{19}{16}, \frac{5}{4}, \frac{3}{2}, 2, \frac{7}{2}$	10

Table 1. Initial condition parameters for computations. Parameters are the non-dimensional channel width (η_o), non-dimensional stand-off distance (γ_o) and initial liquid pressure (p_∞). A baseline case for the channel simulations is considered and compared with the single-wall configuration. Four studies are then considered: (i) dependence on channel width; (ii) initial stand-off distance dependence; (iii) driving pressure ratio dependence; (iv) symmetric domain configuration. Simulations with a single-wall configuration are also computed for comparison.

and $\Delta p = p_\infty - p_o$. Velocities and pressures (including ambient and vapour pressures) are non-dimensionalised using the characteristic re-entrant jet speed, $\sqrt{\Delta p / \rho_\ell}$, and water-hammer pressure, $\rho_\ell a_\ell \sqrt{\Delta p / \rho_\ell}$, respectively (Plesset & Chapman 1971), where a_ℓ is the liquid speed of sound.

The governing equations are mass conservation, momentum and energy balance,

$$\frac{\partial \rho}{\partial t} + \frac{\partial}{\partial x_j}(\rho u_j) = 0, \tag{2.1a}$$

$$\frac{\partial}{\partial t}(\rho u_i) + \frac{\partial}{\partial x_j}(\rho u_i u_j + p \delta_{ij}) = \frac{\partial \tau_{ij}}{\partial x_j}, \tag{2.1b}$$

$$\frac{\partial E}{\partial t} + \frac{\partial}{\partial x_j}((E + p)u_j) = \frac{\partial}{\partial x_k}(u_i \tau_{ik} - Q_k), \tag{2.1c}$$

$$\frac{\partial}{\partial t}(\rho^{(k)} \alpha^{(k)}) + \frac{\partial}{\partial x_j}(\rho^{(k)} \alpha^{(k)} u_j) = 0, \quad k = 1, \ldots, K - 1, \tag{2.1d}$$

where ρ is the total (mixture) density, u_i the velocity vector, τ_{ij} the shear stress tensor, Q_k the heat flux, $\alpha^{(k)}$ is the volume fraction of material k, K is the total number of materials (here, $K = 2$) and indices $i, j = 1, 2$ and 3, where repeated indices denote summation. The total energy (per unit volume) E comprises of internal and kinetic contributions, $E = \rho e + \frac{1}{2}\rho u_k^2$. Material k has volume fraction $\alpha^{(k)}$ and density $\rho^{(k)}$ the following relations, with $\sum_k \rho^{(k)} \alpha^{(k)} = \rho$ and $\sum_k \alpha^{(k)} = 1$. Thus, $K - 1$ mass balance equations, corresponding to the K materials, must be evolved. The internal energy per unit volume is related to the

Phase	n	B (MPa)	b (m^3 kg^{-1})	q (MJ kg^{-1})	c (J (kg K)$^{-1}$)
Vapour	1.47	0	0	2.1	3610
Liquid	1.19	702.8	6.61×10^{-4}	-1.2	955

Table 2. Constants in the Noble–Abel stiffened-gas equation of state for water.

relevant thermodynamic quantities through the Noble–Abel Stiffened gas equation of state of Le Métayer & Saurel (2016),

$$\rho e = \frac{p(1 - \rho b)}{n - 1} + \frac{nB(1 - \rho b)}{n - 1} + \rho q \qquad (2.2a)$$

$$= \rho cT + B(1 - \rho b) + \rho q, \qquad (2.2b)$$

where T is the temperature and q, n, B, b and c are material properties prescribed to produce the correct propagation speeds in liquids and solids (Harlow & Amsden 1971; Le Métayer, Massoni & Saurel 2005; Le Métayer & Saurel 2016). The speed of sound for a substance described by this equation of state is defined as

$$a_\ell = \sqrt{\frac{n(p + B)}{\rho_\ell(1 - \rho_\ell b)}}. \qquad (2.3)$$

Table 2 lists the phenomenological constants for the water phases used in this work. For multiple materials, the calculation of ρe is performed to prevent spurious interfacial errors (Beig & Johnsen 2015).

We include heat diffusion and viscous effects. Fourier conduction describes the heat diffusion process with $Q_k = -\kappa \partial T/\partial x_k$, where κ is the thermal conductivity. Fluids behave in a Newtonian fashion, such that the viscous stress is given by $\tau_{ij} = \mu_b \dot{\epsilon}_{kk}\delta_{ij} + \mu_s \dot{\epsilon}_{ij}^{(d)}$, where μ_b is the bulk viscosity, μ_s the shear viscosity. $\dot{\epsilon}_{ij} = \frac{1}{2}(\partial u_i/\partial x_j + \partial u_j/\partial x_i)$, $\dot{\epsilon}_{ij}^{(d)} = \dot{\epsilon}_{ij} - \frac{1}{3}\dot{\epsilon}_{kk}\delta_{ij}$, is the strain-rate tensor and its deviatoric part, respectively. Since our emphasis is on inertial collapse, surface tension and mass transfer are neglected (Beig 2018). Theoretical simulations using Rayleigh–Plesset-type models, Storey & Szeri (2000) and Preston (2004) suggest that the phase change does not significantly change the inertial collapse dynamics and is also omitted in this study. For water vapour, $\kappa = 0.02$ W (m K)$^{-1}$ and $\mu_b = \mu_s = 10^{-5}$ Pa s; for liquid water, $\kappa = $ W (m K)$^{-1}$ and $\mu_b = \mu_s = 9 \times 10^{-4}$ Pa s. The viscosity and thermal conductivity of the materials are temperature independent in these simulations. The mixture material properties ϕ (e.g. viscosities, thermal conductivities) are weighted by the volume fraction, $\phi = \sum_k \alpha^{(k)}\phi^{(k)}$.

The five-equations multiphase model is used to represent gas/liquid flows (Kapila *et al.* 2001; Allaire, Clerc & Kokh 2002; Murrone & Guillard 2005; Beig & Johnsen 2015). An additional species conservation equation is solved in non-conservative form to maintain interfacial equilibrium conditions for velocity, pressure and temperature (Beig & Johnsen 2015), i.e.

$$\frac{\partial \alpha^{(k)}}{\partial t} + u_j \frac{\partial \alpha^{(k)}}{\partial x_j} = \left(\frac{\alpha^{(k)} \rho^{(k')}(a^{(k')})^2}{\alpha^{(k)} \rho^{(k')}(a^{(k')})^2 + \alpha^{(k')} \rho^{(k)}(a^{(k)})^2} \right) \frac{\partial u_j}{\partial x_j}, \qquad (2.4)$$

where $\alpha^{(k')} = 1 - \alpha^{(k)}$ and k' and k represent the distinct phases and a the speed of sound, $a^2 = n(p + B)/\rho(1 - \rho b)$. For mixture relation for the sound speed, the Wood speed of

sound (Wood & Lindsay 1956) is used to calculate the proximal side term in (2.4) and approximate the Riemann solver wave speeds.

The numerical approach of Beig & Johnsen (2015) is used to solve the governing equations. The third-order accurate total variation diminishing Runge–Kutta scheme of Gottlieb & Shu (1998) is used for time marching with an adaptive time step calculated based on the appropriate advective and diffusion numerical constraints. The convective fluxes are computed in divergence form using a conservative, solution-adaptive approach based on the discontinuity sensor/criterion of Henry de Frahan, Varadan & Johnsen (2015) to discriminate between smooth regions and discontinuities. For smooth regions, standard fourth-order explicit central differences are applied. At discontinuities, the HLL (Harten–Lax–van Leer) Riemann solver (Harten, Lax & van Leer 1983) is used, with proper correction for equations in non-conservative form, detailed by Saurel & Abgrall (1999), in conjunction with the high-order accurate primitive variable WENO (weighted essentially non-oscillatory) reconstruction scheme of Johnsen & Colonius (2006). The first and second derivatives of the diffusion and source terms are computed using explicit fourth-order central differences. The non-zero derivatives of materials properties (i.e. viscosity, thermal conductivity) in mixture regions are calculated using explicit fourth-order accurate central differences.

3. Results and discussion

3.1. *Single-wall and channel comparison*

We compare the qualitative behaviour of bubble collapse in a channel in relation with collapse near a single wall, figure 2 shows contours of pressure (top) and numerical schlieren (bottom) along the centre xz-plane for a bubble collapsing near a single wall (distal) and in a channel of width $\eta_o = 4$ (proximal), with $\gamma_o = 5/4$ (baseline). Given the initial conditions, a rarefaction propagates radially outward (figure 2a1 and figure 2b1). The rarefaction waves from the initial uniform pressure field can affect the bubble collapse dynamics but such effect was not observed, and the surrounding liquid pressure dominates the collapse. The bubble starts to collapse, as shown by the convergence of the flow (figure 2b2). The collapse progression for the channel is similar to the single-wall configuration. However, it takes place at a slower rate due to the rarefaction reflecting off the other channel wall back to the bubble; as a result, the local pressure driving the collapse is reduced by the flow induced by the image bubble. During the collapse and due to the proximity to the proximal wall, a re-entrant jet forms along the distal side of the bubble, directed towards the proximal wall (figure 2a2 and figure 2b3). The jet further penetrates the bubble during collapse and eventually impinges upon the proximal side. Aside from slower collapse rate, the bubble shapes during impingement between the two configurations are qualitatively similar. Upon impingement, an outward-propagating water-hammer shock is emitted and propagates towards the proximal side (figure 2a3 and figure 2b4). Four shock fronts are observed. From left to right, the first shock is the merger of two shocks: re-entrant jet impingement and minimum bubble volume implosion (Beig 2018). These shocks merge into one shock that impinges upon the neighbouring wall. The second is due to the first shock collapsing the vortex ring remnant (frame not shown). The third and fourth shocks are reflections of the first and second from the proximal wall. Comparing the pressure contours between figure 2(a3) and figure 2(b4), the bubble in the channel configuration produces a weaker shock into the surroundings. After these collapse events, the bubble forms into vortex ring convecting towards the proximal wall, as seen by Benjamin & Ellis (1966), Tomita & Shima (1986) and Beig *et al.* (2018) (see figure 2a4).

(*a*)   (*b*)

(*a*1)   (*b*1)

$t/t_c = 0.03$

(*a*2)   (*b*2)

$t/t_c = 0.92$

(*a*3)   (*b*3)

$t/t_c = 1.15$

(*a*4)   (*b*4)

$t/t_c = 1.30$

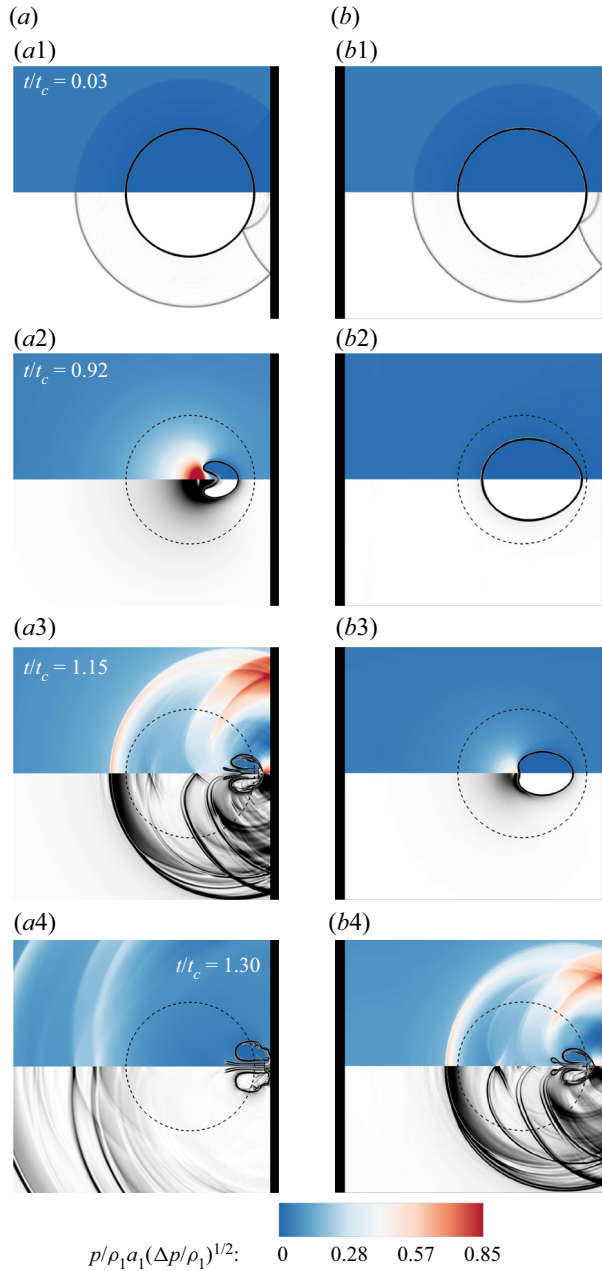$p/\rho_1 a_1 (\Delta p/\rho_1)^{1/2}$:   0   0.28   0.57   0.85

Figure 2. Pressure (top of each panel) and numerical schlieren (bottom of each panel) contours of a bubble along the centre *xz*-plane with $\eta_o = 4$, $\gamma_o = 5/4$ and $p_\infty = 5$ MPa for a single wall (*a*1–*a*4) and channel (*b*1–*b*4). Columns are synchronised in time. Locations are: initial location (---); interface location (——). Movie animations of the simulations are available in the supplementary material available at https://doi.org/10.1017/jfm.2022.571.

To better quantify the energy release upon collapse, figure 3 shows the time history of the bubble volume, migration distance $\Delta x/R_o = \gamma_o - \gamma_c$, and re-entrant jet speed. The three quantities reveal the primary effects of the far channel wall as it slows down the bubble collapse rate in the channel compared with the single-wall configuration. The dynamics
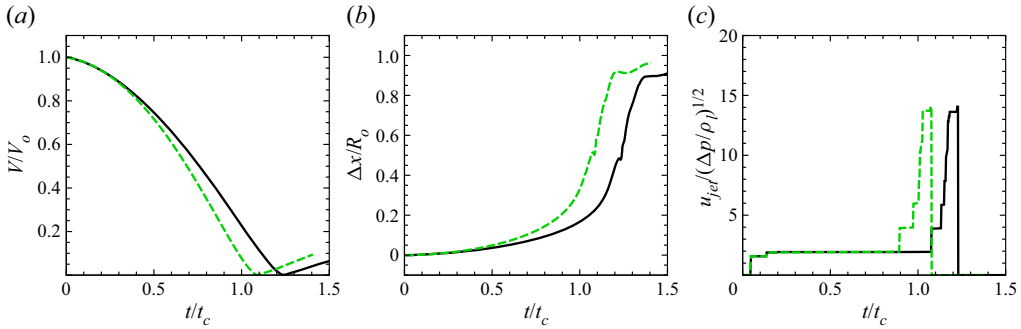
Figure 3. Bubble volume (*a*), migration distance (*b*) and re-entrant jet speed (*c*) versus time, $\eta_o = 4$, $\gamma_o = 5/4$ and $p_\infty = 5$ MPa: channel (——); single wall (- - - -, green).

Configuration	$\min(V/V_o) \times 10^{-3}$	$\Delta x/R_o$
Channel	1.24	0.50
Single wall	1.04	0.55

Table 3. Values of the minimum volume (at collapse) and migration distance at collapse for the channel and single-wall configuration.

are identical until $t/t_c = 0.17$, when the reflected rarefaction impinges upon the bubble in the channel; on this scale, the discrepancy between the channel and single-wall results, due to the impingement of the rarefaction reflected off the second wall, is visible only from $t/t_c \approx 0.4$. Table 3 shows the minimum bubble volume and migration distance at collapse for the channel and single-wall configurations. The larger minimum bubble volume in the channel (compared with the single-wall configuration) yields a weaker water-hammer shock in the liquid. Similarly, the lower migration distance means a larger travel distance for the shock to reach the proximal channel wall and, therefore, weaker (lower) maximum wall pressure relative to the single-wall configuration. The maximum re-entrant jet speeds are $\max(u_{jet})/\sqrt{(\Delta p/\rho_\ell)} = 14.1$ for both configurations.

Figure 4 shows the time history of the non-dimensional pressure at the centreline $x = x_o - W$ (location of the distal wall for the channel or left-hand boundary for single-wall configuration) and $+x_o$ (proximal wall) versus time. As the initial rarefaction reflects off the proximal wall and bubble, the pressure along the proximal wall decreases to reach a minimum $O(10^{-5})$; a similar value is achieved as the initial rarefaction reflects off the far wall of the channel. The pressure then slowly increases until the collapse, at which point the shock thereby produced caused an instantaneous pressure increase, first along the proximal wall since it is closer, then along the far wall (or equivalent location for collapse near a single wall). Additional pressure peaks correspond to the vortex ring collapse shock and reflections. As suggested by the dynamics in figure 3, the shock emission is delayed in the channel compared with the single-wall configuration, again due to the second reflected rarefaction. Given the closer collapse location to the proximal wall (relative to the channel configuration, see table 3) and comparable jet speed, the maximum pressure peaks has a larger magnitude when the collapse takes place near a single wall. Along the far wall (or equivalent location in the case of collapse near a single wall) pressure peaks can be distinguished, though at a smaller magnitude due to the smaller pressure amplitude in
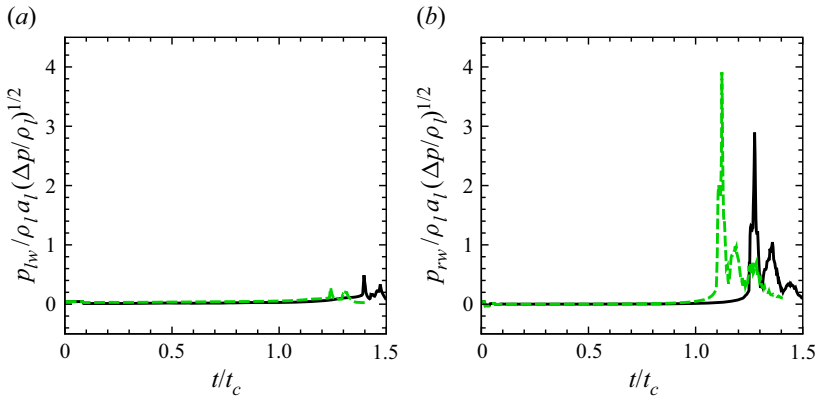
Figure 4. Pressure p_{lw} at $x = x_o - W$ (distal wall in channel, left-hand boundary in single-wall configuration) and p_{rw} at $x = x_o$ (proximal wall) along the centreline versus time, $\eta_o = 4$, $\gamma_o = 5/4$ and $p_\infty = 5$ MPa: channel (——); single wall (----, green).

the direction opposite to the jet and longer distance travelled (Beig 2018). It may seem counter-intuitive that the pressure is higher for the channel far-wall than the single-wall configuration equivalent location. However, there is pressure doubling from the shock impinging on and reflecting from the channel far-wall. In the single-wall configuration, the pressure jump peaks are due to the bubble water-hammer and collapse shock. Considering half the channel wall far-wall maximum pressure (i.e. the maximum pressure in the liquid prior to the shock-wall impingement), the pressure is approximately 12 % less than the maximum wall pressure in the single-wall configuration. This difference is expected due to the larger minimum volume (less intense) at collapse in the channel compared with the single-wall configuration.

3.2. *Dependence on the channel width*

We compare results from simulations with different channel widths η_o to determine the influence of the confinement on the bubble collapse. The driving pressure and initial bubble stand-off distance are fixed to $p_\infty = 5$ MPa and $\gamma_o = 5/4$, respectively. To quantitatively describe the dependence of the collapse on confinement, figure 5 shows the minimum bubble volume at collapse, bubble distance from the wall at collapse and maximum re-entrant jet speed, and figure 6 shows the maximum pressure along the proximal wall for different channel widths. At the larger channel widths (i.e. widths for which the second reflected rarefaction impinges upon the bubble after collapse), these quantities tend to those corresponding to collapse near a single wall at the same initial stand-off distance. For shortest channel width ($\eta_o = 3$), the jet speed is almost twice as high as that corresponding to collapse near a single wall. However, given the $r^{-1.13}$ decay, the larger distance at collapse ($\gamma_c \approx 0.8$ versus 0.7), along with the slightly larger minimum volume, still yields a lower maximum wall pressures compared with collapse near a single wall.

We can readily determine the smallest channel width for which the collapse properties are affected by confinement. The total time for the wave to reach the distal wall, reflect and return to the bubble interface is $t_r = (2d + \Delta x(t_r, \Delta p, \gamma_o))/a_\ell$, where $d = W - (x_o + R_o)$ and is the wave travel distance. To simplify the calculation, we assume the wave is travelling at a constant speed and the speed of sound. The wave travel time (t_r) must be
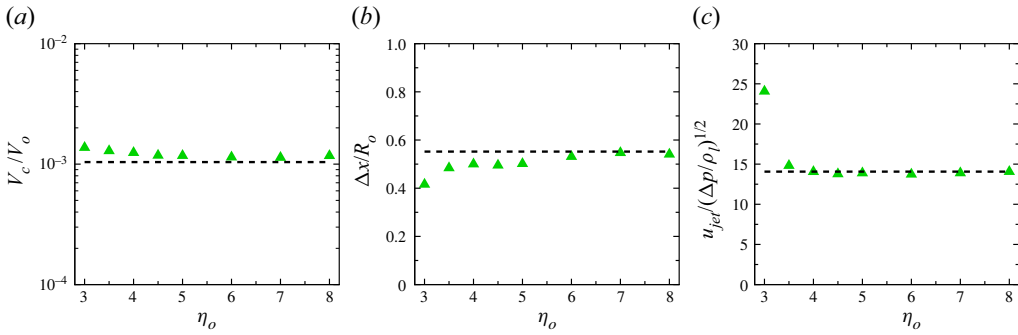
946 A43-10

Figure 5. Minimum bubble volume at collapse (*a*), migration distance (*b*) and maximum re-entrant jet speed (*c*) at collapse versus η_o for $p_\infty = 5$ MPa and $\gamma_o = 5/4$: dashed line (- - -) is the single-wall value.
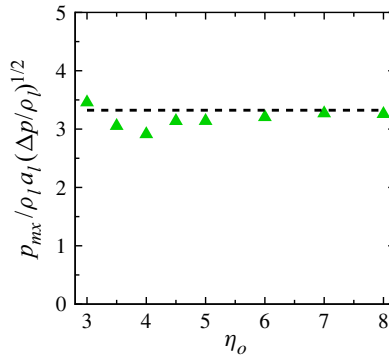

Figure 6. Maximum proximal wall pressures versus η_o for $p_\infty = 5$MPa and $\gamma_o = 5/4$: dashed line (---) is the single-wall value.

less than the single-wall bubble collapse time (t_{sc}), i.e. $t_r/t_{sc} < 1$; otherwise, the wave does not return in time to affect the collapse dynamics. The single-wall bubble collapse time is greater than the Rayleigh collapse time such that $t_{sc} = ft_c$ with factor $f > 1$. Rearranging the expression for the t_r/t_{sc} ratio, we obtain the inequality for the channel width at which it no longer affects a bubble collapse,

$$\eta_o > \gamma_o + 1 + \frac{1}{2}\left[0.915f\sqrt{\frac{n(p_{atm} + B)}{\Delta p}} - \frac{\Delta x}{R_o}\right]. \tag{3.1}$$

For $p_\infty = 5$ MPa and $\gamma_o = 5/4, f = 1.24$ (see figure 3), $t_c = 6.7$ μs and $\Delta x \approx 0.5R_o$ (see figure 3 and table 3). Thus, for the baseline case of parameters, the channel width must be $\eta_o \gtrsim 9.4$ (or $W \gtrsim 9.4R_o$) to no longer affect the bubble collapse. For an attached bubble (e.g. $\gamma_o = -1$), (3.1) yields the $\eta_o > 7$ observation of Gonzalez-Avila *et al.* (2011).

3.3. *Initial stand-off distance dependence*

To better understand the role of the second wall, we examine simulations with different initial stand-off distances γ_o while holding the channel width fixed at $\eta_o = 4$. To quantify the intensity of the collapse, figure 7 shows the minimum bubble volume, maximum
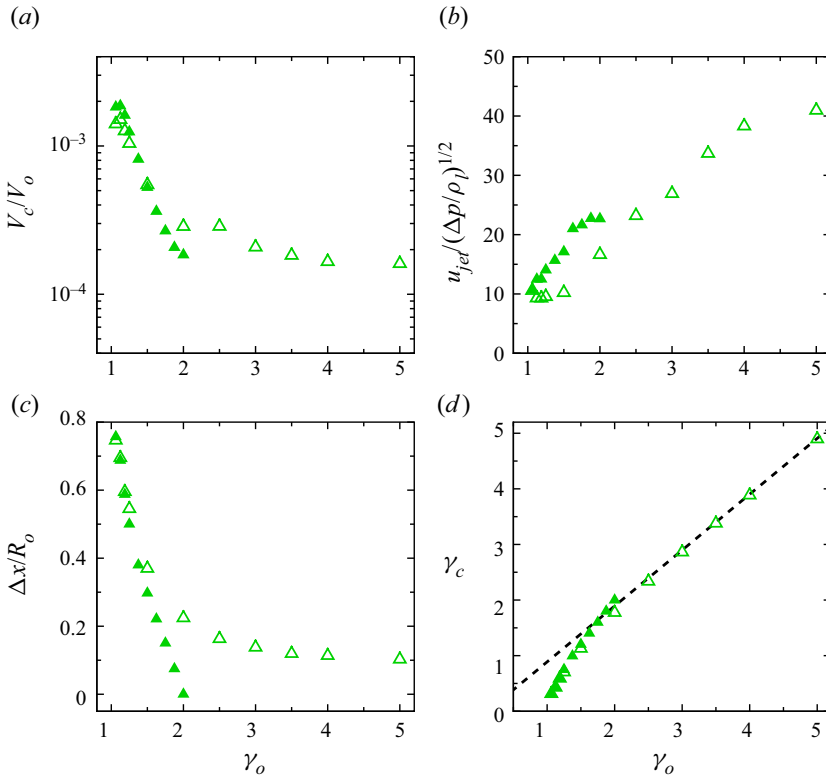
Figure 7. Minimum bubble volume at collapse (*a*), maximum re-entrant jet speed (*b*), migration distance (*c*) and collapse location (*d*) versus γ_o for $p_\infty = 5$ MPa and $\eta_o = 4$: channel (▲, green); single wall (△, green); dashed black line (---) slope 1.

re-entrant jet speed, migration distance and collapse location for different initial bubble stand-off locations. The smallest minimum volume is achieved under symmetric collapse, i.e. $\gamma_o = \gamma_c = 2$. This is attributed to the increased inertia from the two impinging jets (discussed in § 3.1) compressing the bubble into a smaller volume compared with the single jet cases. Moreover, the collapse volume for the channel is comparable to the single-wall $\gamma_o = 5$ case for which the collapse is near spherical. For $\gamma_o < 3/2$ the collapse is affected early enough by the rarefactions reflected by both walls, which reduce the driving pressure and thus the intensity of the collapse.

Over the course of its collapse, the bubble is attracted to various degrees by the image sinks representing the walls, and therefore migrate. For this channel width, bubbles initially close to the wall migrate significantly towards the wall, by an amount similar to their single-wall counterparts. For $\gamma_o \gtrsim 3/2$, the influence of the far wall is greater, resulting in less migration towards the wall than in collapse near a wall. A consequence is that bubbles at the largest initial stand-off distances have collapse locations farther from the wall than the corresponding collapse near a single wall. In other words, the shock is emitted at a farther distance from the proximal wall in the presence of a second wall. With smaller volumes, higher local velocities (including jet speeds) are achieved for $\gamma_o \gtrsim 3/2$ (see figure 7). Thus, a stronger water-hammer shock is emitted into the liquid in these cases.
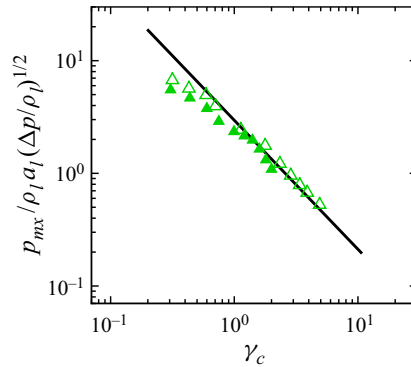
Figure 8. Maximum proximal wall pressures versus γ_c for $p_\infty = 5\text{MPa}$ and $\eta_o = 4$: channel (▲, green); single wall (△, green); solid black line (——) is slope -1.13 observed for underwater explosion shocks (Cole 1948).

Figure 8 shows the maximum pressure, p_{mx}, along the proximal channel wall from the water-hammer shock versus the location of the bubble collapse since this location – rather than the initial stand-off distance – is representative of the spatial origin of the emitted shock. We note that the same γ_o for the single-wall and channel cases were considered. However, due to the different dynamics produced by different levels of confinement, the bubble collapse locations γ_c are different between the two configurations. The maximum wall pressure is highest for those bubbles collapsing nearest to the wall, and decreases as the collapse distance from the wall (and thus initial stand-off distance, see figure 7c,d) is increased, following an $r^{-1.13}$ scaling consistent with underwater explosions (Cole 1948) and bubble collapse near a single wall (Beig 2018). Consistent with the observations about the minimum volume and jet speed, the increased effect of the second wall, i.e. its proximity, gives rise to a lower maximum wall pressure along the proximal wall compared with a bubble collapsing near a single wall: as $\gamma_o \to 1$, the bubble collapses close to the proximal wall and the jet speeds are comparable to their single-wall counterparts; however, emitted shocks are weaker, and thus the maximum wall pressures are lower, due to the larger minimum bubble volume at collapse. At larger stand-off distances, though the jet speed (and thus the strength of the emitted shock) is higher and minimum volume smaller, the collapse occurs at a distance farther from the proximal wall in bubble collapse in a channel; the $r^{-1.13}$ decay of the shock amplitude thus gives rise to a lower wall pressure. We also note that the bubbles closer to channel centre produce higher pressures along the far (distal) wall due to being closer to the wall upon collapse.

3.4. *Driving pressure ratio dependence*

We examine how the driving pressure ratio affects the bubble dynamics. The channel width is fixed to $\eta_o = 4$ and the initial bubble stand-off distance is varied. Figure 9 shows the bubble collapse volume, maximum re-entrant jet speed, migration distance and collapse location for different initial bubble stand-off distances, three driving pressures and channel and single-wall configurations. The minimum volume and migration distance data for each respective configuration (single-wall versus channel) follow a similar behaviour as discussed in § 3.3. For the collapse in a channel, the higher driving pressures give rise to smaller minimum volume for bubbles initially near the middle of the channel, and larger minimum volumes for bubbles closer to the proximal wall.
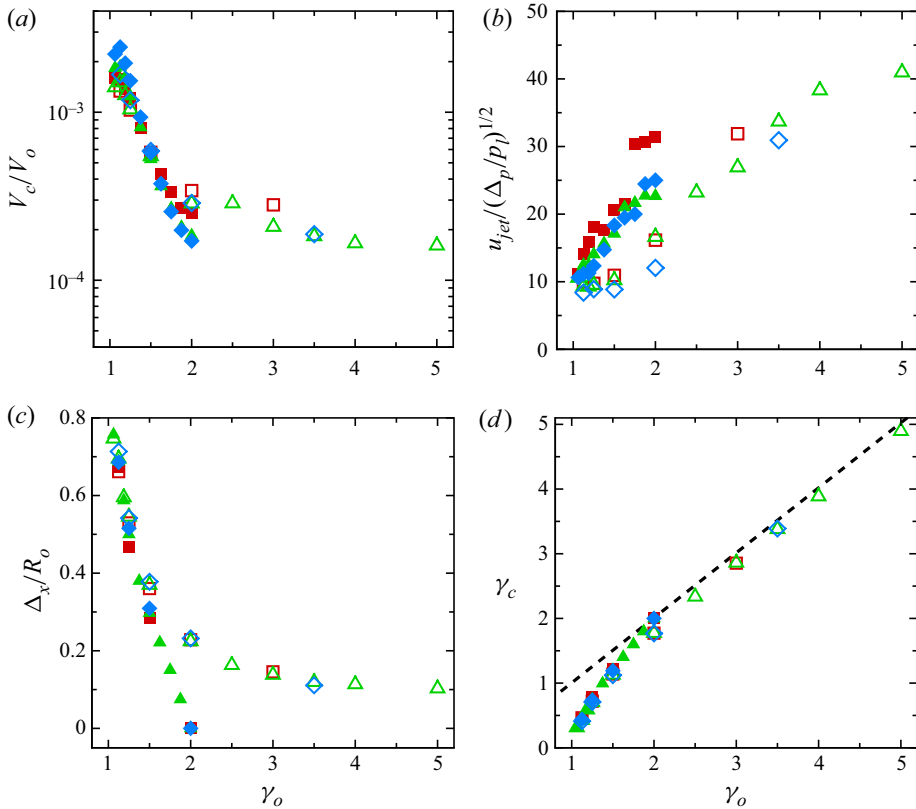
Figure 9. Minimum bubble volume at collapse (*a*), maximum re-entrant jet speed (*b*), migration distance (*c*) and collapse location (*d*) versus γ_o with $\eta_o = 4$ for p_∞: 2 (channel, ■ red; single wall, □ red); 5 (channel, ▲ green; single wall, △ green); and 10 MPa (channel, ◇ filled blue; single wall, ◇ blue). The dashed black line (---) is slope 1.

For $\gamma_o \gtrsim 3/2$, the migration is small because the bubble location is closer to the middle of the channel, such that the effect of the far wall becomes comparable to that of the proximal wall, thus leading to a more symmetric (about the centreplane parallel to the walls) collapse. The re-entrant jets follow inverse trends and still obey the water-hammer scaling.

The maximum wall pressure along the distal and proximal wall versus collapse location for the three driving pressures is shown in figure 10. Trends similar to the $p_\infty = 5$ MPa case in § 3.3 are observed. Both distal and proximal maximum wall pressures follow the black solid curve for underwater explosion shock decay (Cole 1948). The maximum wall pressures along the proximal wall are lower in the channel configuration than in collapse near a single wall for the same initial stand-off distance. For a sufficiently large initial stand-off distance, this maximum pressure is appropriately scaled by the water-hammer speed/pressure (see distal wall maximum pressures). In summary, increasing the driving pressure while keeping the other parameters fixed both speeds up the collapse and produces a more intense collapse as evidenced by the higher jet speed and smaller minimum volume, thus leading to higher proximal wall pressures. Additionally, there is a larger range of stand-off distances for which bubbles are not affected by the second wall since the collapse time is faster.
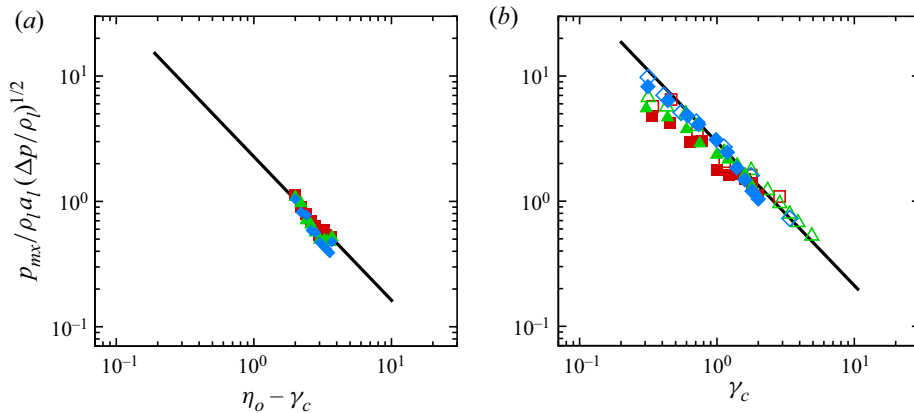
Figure 10. Maximum far (*a*) and proximal (*b*) wall pressures versus collapse location with $\eta_o = 4$ for p_∞: 2 (channel, ■ red; single wall, □ red); 5 (channel, ▲ green; single wall, △ green); and 10 MPa (channel, ◇ filled blue; single wall, ◇ blue). The solid black line (——) is slope -1.13 observed for underwater explosions (Cole 1948).

3.5. *Symmetric domain configuration*

We examine the configuration of a channel-centred bubble as the channel width is varied. The aim is to determine the channel width at which the collapse dynamics change and quantify the corresponding maximum wall pressures. The channel width, initial bubble stand-off distance and collapse location are related such that $\gamma_o = \gamma_c = \eta_o/2$. Figure 11 shows the non-dimensional pressure and numerical schlieren contours for $\eta_o = 9/4$ (figure 11*a*1–*a*3), 3 (figure 11*b*1–*b*3) and 7/2 (figure 11*c*1–*c*3). For $\eta_o = 9/4$, the proximity of the bubble walls to the channel walls prevents wall-normal (horizontal) re-entrant jet formation due the attraction from the image bubbles (see figure 11*a*1). That is, the channel wall boundary conditions inhibit the liquid surroundings to fill the previously occupied space by the gas bubble as the bubble collapses in the horizontal direction. The bubble continues to collapse with re-entrant jets forming in the wall-parallel (vertical) direction (figure 11*a*2) as observed by Chahine (1982) and Kucera & Blake (1990). The re-entrant jets impinge on each other yielding a water-hammer shock (figure 11*a*3). Vortex rings form and stretch horizontally, collapse due to the incident water-hammer shock, and emit water-hammer shocks of their own closer to the walls relative the bubble initial location. At the critical channel width $\eta_o \approx 3$, the vertical and horizontal sides of the bubble collapse at a similar rate (figure 11*b*2). However, the collapse is not spherical, and the bubble forms wall-normal at collapse, converging re-entrant jets. The jets impinge at the channel centre and horizontal vortex rings are not observed. A different collapse morphology takes place for $\eta_o = 7/2$. The jet direction goes from wall-parallel to wall-normal. Angled jets are not observed for intermediate channel widths. The surrounding liquid fills the space in the horizontal direction as the bubble collapses (see figure 11*b*2). Two horizontal jets form and impinge on each other at the channel centre yielding the outward-propagating shock (figure 11*b*2). The vortex ring's normal direction is horizontal and stretches in the vertical direction. After the collapse, the resulting shocks travel across the channel, reflect from the walls towards the ring (figure 11*b*3).

Figure 12 shows the non-dimensional minimum bubble volume as a function of initial stand-off distance (and channel width since $\gamma_o = \eta_o/2$). As the stand-off distance increases, the liquid surroundings fill the space as the bubble collapses towards
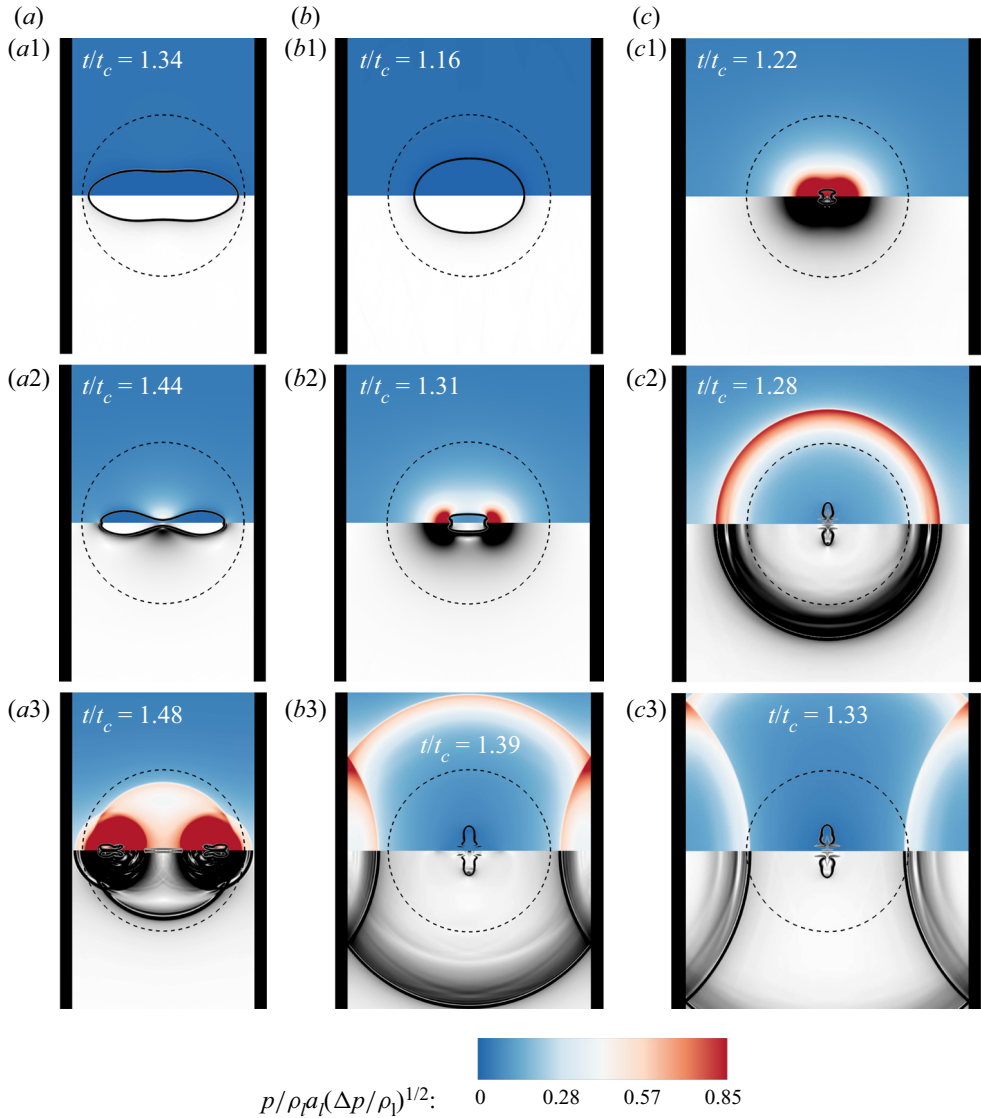
Figure 11. Pressure (top of each panel) and numerical schlieren (bottom of each panel) contours along the centre xz-plane for bubble centred in the channel with $p_\infty = 5$ MPa and confinement $\eta_o = 9/4$ ($a1$–$a3$), 3 ($b1$–$b3$) and $7/2$ ($c1$–$c3$): initial location (- - -); interface location (——). Movie animations of the simulations are available in the supplementary material.

the centroid. Then, converging horizontal jets compress the gas to a volume smaller than the single-wall cases for the same γ_o. However, as seen before, the larger distance from the channel walls reduces the maximum wall pressures.

The maximum wall pressure for the channel-centred bubble versus collapse location are shown in figure 13 (alongside the single-wall values). If we consider $\gamma_c = \gamma_o$ for these configurations, the critical channel width for horizontal-to-vertical jetting is observed at $\eta_o \approx 3$. The critical channel width is comparable to that observed by Chahine (1982) of $\eta_o \approx 20/9$. Despite the limitation of the weakly compressible assumption, boundary-element methods may be able to accurately quantify the transition η_o in
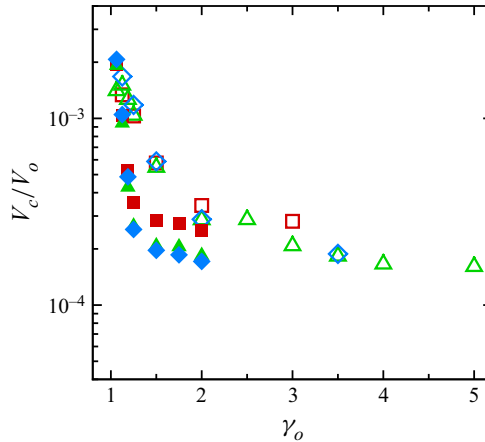
946 A43-16

Figure 12. Minimum bubble volume at collapse versus γ_o for p_∞: 2 (channel, ■ red; single wall, □ red); 5 (channel, ▲ green; single wall, △ green); and 10 MPa (channel, ◇ filled blue; single wall, ◇ blue).
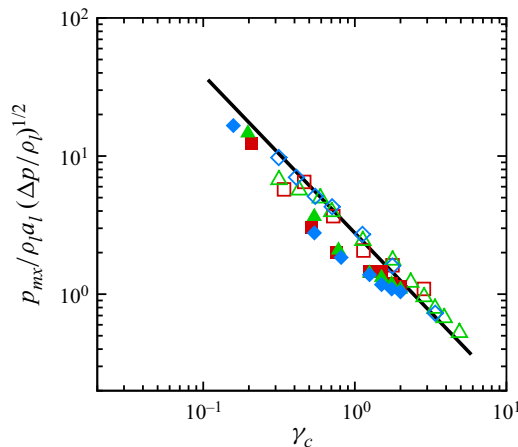

Figure 13. Maximum proximal wall pressure versus collapse location for p_∞: 2 (channel, ■ red; single wall, □ red); 5 (channel, ▲ green; single wall, △ green); and 10 MPa (channel, ◇ filled blue; single wall, ◇ blue). The solid black line (——) slope is -1.13 observed for underwater explosion shocks (Cole 1948).

the absence of the compressible flow dynamics (Hsiao *et al.* 2013). For $\eta_o \leqslant 5/2$, the wall-parallel re-entrant jets strengthen the collapse of the resulting vortex ring. The proximity of the vortex-ring remnants to the walls yields higher maximum wall pressures than the single-wall cases if $\gamma_o = \gamma_c$. Instead, we consider the bubble remnant collapse location (see figure 11*a*3) in figure 13. We note that for $\eta_o \leqslant 5/2$, the vortex ring remnant collapse location is $\gamma_c \approx 4(\gamma_o - 1)$. The non-dimensional maximum wall pressure amplitude decay of $1/r^{1.13}$ is retained with these collapse locations. For $\eta_o > 5/2$, the maximum channel wall pressures follow the pressure scaling with $\gamma_c = \gamma_o$.

4. Conclusions

Numerical simulations were conducted to understand the role of confinement on the dynamics and pressures generated by a single inertially collapsing bubble between rigid,

946 A43-17

parallel walls (channel). As the bubble collapses, rarefaction waves propagate radially outward, reflect off both walls (typically at separate times depending on the bubble location and channel size), and interact with the bubble again. A re-entrant jet directed towards the proximal wall forms, impinges upon the opposite side of the bubble, and generates a water-hammer shock that impinges upon the proximal wall. The presence of the second wall changes the pressure field during collapse compared with the corresponding collapse near a single wall; in particular, the pressure on the distal side of the bubble (farthest from the proximal wall) is reduced, thus generally reducing the intensity of the collapse (larger minimum volume and farther distance to the wall at collapse). For a fixed initial stand-off distance, as the channel width increases, i.e. $\eta_o \to \infty$, the bubble volume, migration distance and re-entrant jet speed approach their single-wall counterparts. The maximum wall pressure, however, monotonically approached a value below observed in the single-wall case due to the modified the pressure field in the channel.

Varying stand-off distance reduced the maximum wall pressures in the channel relative to the single wall. For $\gamma_o \lesssim 3/2$, the collapse was less intense due to the proximity to the wall (attraction to image bubble). For $\gamma_o \gtrsim 3/2$, the collapse was intensified (i.e. smaller minimum volume and higher re-entrant jet speed); however, the bubble collapses farther away from the channel walls such that the water-hammer shock pressure decayed below the single-wall value. The stand-off distance observations are consistent for three different driving pressures. Two different jetting behaviours are seen for a channel-centred bubble collapse. Horizontal re-entrant jets form for channel widths greater than the critical channel width $\eta_o \approx 3$. For $\eta_o \leqslant 5/2$, wall-parallel (vertical) re-entrant jets impinged at the bubble centroid strengthening the remnant vortex ring's collapse due to the channel walls sufficiently restricting the bubble's horizontal motion (image bubbles) such that the vertical direction collapse dominates the flow morphology. By accounting for bubble remnant collapse location, the maximum pressure decay of $1/r^{1.13}$ was observed. Future studies will consider the inertial collapse of wall-attached bubbles to compare with the results of Hsiao *et al.* (2014) and Zeng *et al.* (2020).

Supplementary material and movies. Supplementary material and movies are available at https://doi.org/10.1017/jfm.2022.571.

Declaration of interests. The authors report no conflict of interest.

Author ORCIDs.
- Mauro Rodriguez Jr https://orcid.org/0000-0003-0545-0265;
- Shahaboddin A. Beig https://orcid.org/0000-0002-6865-4858;
- Eric Johnsen https://orcid.org/0000-0001-9530-408X.

REFERENCES

AGANIN, A.A., ILGAMOV, M.A., KOSOLAPOVA, L.A. & MALAKHOV, V.G. 2016 Dynamics of a cavitation bubble near a solid wall. *Thermophys. Aeromech.* **23**, 211–220.

ALLAIRE, G., CLERC, S. & KOKH, S. 2002 A five-equation model for the simulation of interfaces between compressible fluids. *J. Comput. Phys.* **181**, 577–616.

BEIG, S.A. 2018 A computational study of the inertial collapse of gas bubbles near a rigid surface. PhD thesis, University of Michigan, Ann Arbor.

BEIG, S.A., ABOULHASANZADEH, B. & JOHNSEN, E. 2018 Temperatures produced by inertially collapsing bubbles near rigid surfaces. *J. Fluid Mech.* **852**, 105–125.

BEIG, S.A. & JOHNSEN, E. 2015 Maintaining interface equilibrium conditions in compressible multiphase flows using interface capturing. *J. Comput. Phys.* **302**, 548–566.

BENJAMIN, T.B. & ELLIS, A.T. 1966 The collapse of cavitation bubbles and the pressures thereby produced against solid boundaries. *Phil. Trans. R. Soc. Lond.* A **260**, 221–240.

BLAKE, J.R. & GIBSON, D.C. 1987 Cavitation bubbles near boundaries. *Annu. Rev. Fluid Mech.* **19**, 99–123.

BLAKE, J.R., TAIB, B.B. & DOHERTY, G. 1986 Transient cavities near boundaries. Part 1. Rigid boundary. *J. Fluid Mech.* **170**, 479–497.

BRUJAN, E.A., KEEN, G.S., VOGEL, A. & BLAKE, J.R. 2002 The final stage of the collapse of a cavitation bubble close to a rigid boundary. *Phys. Fluids* **14**, 85–92.

BRUJAN, E.-A., NODA, T., ISHIGAMI, A., OGASAWARA, T. & TAKAHIRA, H. 2018 Dynamics of laser-induced cavitation bubbles near two perpendicular rigid walls. *J. Fluid Mech.* **841**, 28–49.

BRUJAN, E.A., TAKAHIRA, H. & OGASAWARA, T. 2019 Planar jets in collapsing cavitation bubbles. *Exp. Therm. Fluid Sci.* **101**, 48–61.

CHAHINE, G.L. 1982 Experimental and asymptotic study of nonspherical bubble collapse. *Appl. Sci. Res.* **38**, 187–197.

CHAHINE, G.L. & MORINE, A.K. 1980 Collapse d'une bulle de cavitation entre deux parois solides. In *Proceedings of the 4th International Meeting Water-Column Separation*, pp. 79–101.

COLE, R.H. 1948 *Underwater Explosions*. Princeton University Press.

CORALIC, V. & COLONIUS, T. 2013 Shock-induced collapse of a bubble inside a deformable vessel. *Eur. J. Mech.* (B/*Fluids*) **40**, 64–74.

DABIR-MOGHADDAM, N. & WU, B. 2016 Effects of microhole sidewall confinement on bubble growth and bubble-generated shock waves. *J. Manuf. Process.* **22**, 229–236.

FARHANGMEHR, V., HAJIZADEH AGHDAM, A., SHERVANI-TABAR, M.T., PARVIZI, R., OHL, S.W. & KHOO, B.C. 2014 Numerical investigation on the pulsating bubble dynamics in a narrow cylinder with a compliant coating. *Fluid Dyn. Res.* **46**, 015513.

FRANC, J.-P., RIONDET, M., KARIMI, A. & CHAHINE, G.L. 2011 Impact load measurements in an erosive cavitating flow. *Trans. ASME J. Fluids Engng* **133**, 121301.

FRANC, J.-P., RIONDET, M., KARIMI, A. & CHAHINE, G.L. 2012 Material and velocity effects on cavitation erosion pitting. *Wear* **274–275**, 248–259.

FUTAKAWA, M., NAOE, T., KOGAWA, H., HAGA, K. & OKITA, K. 2014 Cavitation erosion induced by proton beam bombarding mercury target for high-power spallation neutron sources. *Exp. Therm. Fluid Sci.* **57**, 365–370.

GONZALEZ-AVILA, S.R., VAN BLOKLAND, A.C., ZENG, Q. & OHL, C.-D. 2019 Jetting and shear stress enhancement from cavitation bubbles collapsing in a narrow gap. *J. Fluid Mech.* **884**, 1–23.

GONZALEZ-AVILA, S.R., KLASEBOER, E., KHOO, B.C. & OHL, C.-D. 2011 Cavitation bubble dynamics in a liquid gap of variable height. *J. Fluid Mech.* **682**, 241–260.

GOTTLIEB, S. & SHU, C.-W. 1998 Total variation diminishing Runge–Kutta schemes. *Maths. Comput.* **67**, 73–85.

HAINES, J.R., MCMANAMY, T.J., GABRIEL, T.A., BATTLE, R.E., CHIPLEY, K.K., CRABTREE, J.A., JACOBS, L.L., LOUSTEAU, D.C., RENNICH, M.J. & RIEMER, B.W. 2014 Spallation neutron source target station design, development, and commissioning. *Nucl. Instrum. Meth. Phys. Res.* **764**, 94–115.

HARLOW, F.H. & AMSDEN, A.A. 1971 *Fluid Dynamics*. Los Alamos Scientific Laboratory.

HARTEN, A., LAX, P.D. & VAN LEER, B. 1983 On upstream differencing and godunov-type schemes for hyperbolic conservation laws. *SIAM Rev.* **25**, 35–61.

HENRY DE FRAHAN, M.T., VARADAN, S. & JOHNSEN, E. 2015 A new limiting procedure for discontinuous Galerkin methods applied to compressible multiphase flows with shocks and interfaces. *J. Comput. Phys.* **280**, 489–509.

HICKLING, R. & PLESSET, M.S. 1964 Collapse and rebound of a spherical bubble in water. *Phys. Fluids* **7**, 7–14.

HSIAO, C.-T., JAYAPRAKASH, A., KAPAHI, A., CHOI, J.-K. & CHAHINE, G.L. 2014 Modelling of material pitting from cavitation bubble collapse. *J. Fluid Mech.* **755**, 142–175.

HSIAO, C.-T.T., *et al.* 2013 Modelling single- and tandem-bubble dynamics between two parallel plates for biomedical applications. *J. Fluid Mech.* **716**, 137–170.

ISHIDA, H., NUNTADUSIT, C., KIMOTO, H., NAKAGAWA, T. & YAMAMOTO, T. 2001 Cavitation bubble behavior near solid boundaries. In *Fourth International Symposium on Cavitation*, pp. 1–8.

JOHNSEN, E. & COLONIUS, T. 2006 Implementation of WENO schemes in compressible multicomponent flow problems. *J. Comput. Phys.* **219**, 715–732.

KAPILA, A.K., MENIKOFF, R., BDZIL, J.B., SON, S.F. & STEWART, D.S. 2001 Two-phase modeling of deflagration-to-detonation transition in granular materials: reduced equations. *Phys. Fluids* **13**, 3002–3024.

KIM, K.-H., CHAHINE, G., FRANC, J.-P. & KARIMI, A. (Ed.) 2014 *Advanced Experimental and Numerical Techniques for Cavitation Erosion Prediction*, Fluid Mechanics and its Applications, vol. 106. Springer.

KORNFELD, M. & SUVOROV, L. 1944 On the destructive action of cavitation. *J. Appl. Phys.* **15**, 495–506.

KUCERA, A. & BLAKE, J.R. 1990 Approximate methods for modelling cavitation bubbles near boundaries. *Bull. Austral. Math. Soc.* **41**, 1–44.

KUVSHINOV, G.I., PROKHORENKO, P.P., DEZHKUNOV, N.V. & KUVSHINOV, V.I. 1982 Collapse of a cavitation bubble between two solid walls. *Intl J. Heat Mass Transfer* **25**, 381–387.

LAUTERBORN, W. & BOLLE, H. 1975 Experimental investigations of cavitation-bubble collapse in the neighbourhood of a solid boundary. *J. Fluid Mech.* **72**, 391–399.

LE MÉTAYER, O., MASSONI, J. & SAUREL, R. 2005 Modelling evaporation fronts with reactive Riemann solvers. *J. Comput. Phys.* **205**, 567–610.

LE MÉTAYER, O. & SAUREL, R. 2016 The Noble–Abel Stiffened–Gas equation of state. *Phys. Fluids* **28**, 046102.

LI, S.M., ZHANG, A.M., WANG, Q.X. & ZHANG, S. 2019 The jet characteristics of bubbles near mixed boundaries. *Phys. Fluids* **31**, 107105.

MCCLINTOCK, D.A., RIEMER, B.W., FERGUSON, P.D., CARROLL, A.J. & DAYTON, M.J. 2012 Initial observations of cavitation-induced erosion of liquid metal spallation target vessels at the Spallation Neutron Source. *J. Nucl. Mater.* **431**, 147–159.

MOLEFE, L. & PETERS, I.R. 2019 Jet direction in bubble collapse within rectangular and triangular channels. *Phys. Rev.* E **100**, 063105.

MURRONE, A. & GUILLARD, H. 2005 A five equation reduced model for compressible two phase flow problems. *J. Comput. Phys.* **202**, 664–698.

NAOE, T., KOGAWA, H., WAKUI, T., HAGA, K., TESHIGAWARA, M., KINOSHITA, H., TAKADA, H. & FUTAKAWA, M. 2016 Cavitation damage prediction for the JSNS mercury target vessel. *J. Nucl. Mater.* **468**, 313–320.

NAOE, T., WAKUI, T., KINOSHITA, H., KOGAWA, H., HAGA, K., HARADA, M., TAKADA, H. & FUTAKAWA, M. 2018 Cavitation damage in double-walled mercury target vessel. *J. Nucl. Mater.* **506**, 35–42.

NAUDÉ, C.F. & ELLIS, A.T. 1961 On the mechanism of cavitation damage by nonhemispherical cavities collapsing in contact with a solid boundary. *Trans. ASME J. Basic Engng* **83**, 648–656.

OĞUZ, H.N. & PROSPERETTI, A. 1998 The natural frequency of oscillation of gas bubbles in tubes. *J. Acoust. Soc. Am.* **103**, 3301–3308.

PHILIPP, A. & LAUTERBORN, W. 1998 Cavitation erosion by single laser-produced bubbles. *J. Fluid Mech.* **361**, 75–116.

PLESSET, M.S. & CHAPMAN, R.B. 1971 Collapse of an initially spherical vapour cavity in the neighbourhood of a solid boundary. *J. Fluid Mech.* **47**, 283–290.

PRESTON, A.T. 2004 Modeling heat and mass transfer in bubbly cavitating flows and shock waves in cavitating nozzles. PhD thesis, California Institute of Technology.

RAYLEIGH, LORD 1917 On the pressure developed in a liquid during the collapse of a spherical cavity. *Phil. Mag.* **34**, 94–98.

RIEMER, B.W., MCCLINTOCK, D.A., KAMINSKAS, S. & ABDOU, A.A. 2014 Correlation between simulations and cavitation-induced erosion damage in Spallation Neutron Source target modules after operation. *J. Nucl. Mater.* **450**, 183–191.

SAGAR, H.J. & EL MOCTAR, O. 2020 Dynamics of a cavitation bubble near a solid surface and the induced damage. *Trans. ASME J. Fluids Struct.* **92**, 102799.

SAUREL, R. & ABGRALL, R. 1999 A simple method for compressible multifluid flows. *SIAM J. Sci. Comput.* **21**, 1115–1145.

SCHMIDMAYER, K., BRYNGELSON, S.H. & COLONIUS, T. 2020 An assessment of multicomponent flow models and interface capturing schemes for spherical bubble dynamics. *J. Comput. Phys.* **402**, 109080.

STOREY, B.D. & SZERI, A.J. 2000 A reduced model of cavitation physics for use in sonochemistry. *J. Acoust. Soc. Am.* **107**, 2866.

SUPPONEN, O., OBRESCHKOW, D., KOBEL, P., TINGUELY, M., DORSAZ, N. & FARHAT, M. 2017 Shock waves from nonspherical cavitation bubbles. *Phys. Rev. Fluids* **2**, 093601.

SUPPONEN, O., OBRESCHKOW, D., TINGUELY, M., KOBEL, P., DORSAZ, N. & FARHAT, M. 2016 Scaling laws for jets of single cavitation bubbles. *J. Fluid Mech.* **802**, 263–293.

THOMPSON, K.W. 1990 Time-dependent boundary conditions for hyperbolic systems, II. *J. Comput. Phys.* **89**, 439–461.

TOMITA, Y. & SHIMA, A. 1986 Mechanisms of impulsive pressure generation and damage pit formation by bubble collapse. *J. Fluid Mech.* **169**, 535–564.

TRUMMLER, T., BRYNGELSON, S.H., SCHMIDMAYER, K., SCHMIDT, S.J., COLONIUS, T. & ADAMS, N.A. 2020 Near-surface dynamics of a gas bubble collapsing above a crevice. *J. Fluid Mech.* **899**, A16.

TRUMMLER, T., SCHMIDT, S.J. & ADAMS, N.A. 2021 Effect of stand-off distance and spatial resolution on the pressure impact of near-wall vapor bubble collapses. *Intl J. Multiphase Flow* **141**, 103618.

VINCENT, O. & MARMOTTANT, P. 2017 On the statics and dynamics of fully confined bubbles. *J. Fluid Mech.* **827**, 194–224.

VINCENT, O., MARMOTTANT, P., GONZALEZ-AVILA, S.R., ANDO, K. & OHL, C.D. 2014 The fast dynamics of cavitation bubbles within water confined in elastic solids. *Soft Matt.* **10**, 1455–1461.

VOGEL, A., LAUTERBORN, W. & TIMM, R. 1989 Optical and acoustic investigations of the dynamics of laser-produced cavitation bubbles near a solid boundary. *J. Fluid Mech.* **206**, 299–338.

WANG, Q.X. 2014 Multi-oscillations of a bubble in a compressible liquid near a rigid boundary. *J. Fluid Mech.* **745**, 509–536.

WOOD, A.B. & LINDSAY, R.B. 1956 A textbook of sound. *Phys. Today* **9**, 37–37.

ZENG, Q., GONZALEZ-AVILA, S.R. & OHL, C.-D. 2020 Splitting and jetting of cavitation bubbles in thin gaps. *J. Fluid Mech.* **896**, A28.

ZHANG, S., DUNCAN, J.H. & CHAHINE, G.L. 1993 Simulation of the final stage of bubble collapse near a rigid wall. *Trans. ASME J. Fluids Engng* **257**, 147–181.